Earth, Planets and Space

FULL PAPER Open Access

Space weather impacts on the ionosphere over the southern African mid-latitude region

Tshimangadzo Merline Matamba[1*], Donald W. Danskin[1], Rendani R. Nndanganeni[1] and Mpho Tshisaphungo[1]

Abstract

The ionosphere suffers major perturbations during severe space weather events such as Coronal Mass Ejections (CMEs), solar flares, high-speed streams, and Corotating Interaction Regions (CIRs). The ionosphere can experience depletions or enhancements in Total Electron Content (TEC) during severe space weather conditions. The South African National Space Agency (SANSA) near-real-time (NRT) TEC maps were used to show the ionospheric variability during the geomagnetic storm of 3–8 Nov 2021 over the southern Africa mid-latitude region. The ionosonde TEC, NRT TEC, and the quiet-time AfriTEC model were compared during the 6-day period. A negative ionospheric response was observed during the main and recovery phases of the geomagnetic storm (4–5 Nov 2021). The changes to neutral composition O/N_2 was one of the physical processes attributed to the decrease in TEC over the mid-latitude region. The GPS TEC maps showed a very good agreement with ionosonde measurements and the AfriTEC model. A strong east–west TEC gradient was observed occurring between two ionosonde stations.

Keywords Ionospheric storms, Geomagnetic storms, Ionosphere, Total electron content, TEC gradient

*Correspondence:
Tshimangadzo Merline Matamba
mtshimangadzo@sansa.org.za
Full list of author information is available at the end of the article

Graphical Abstract

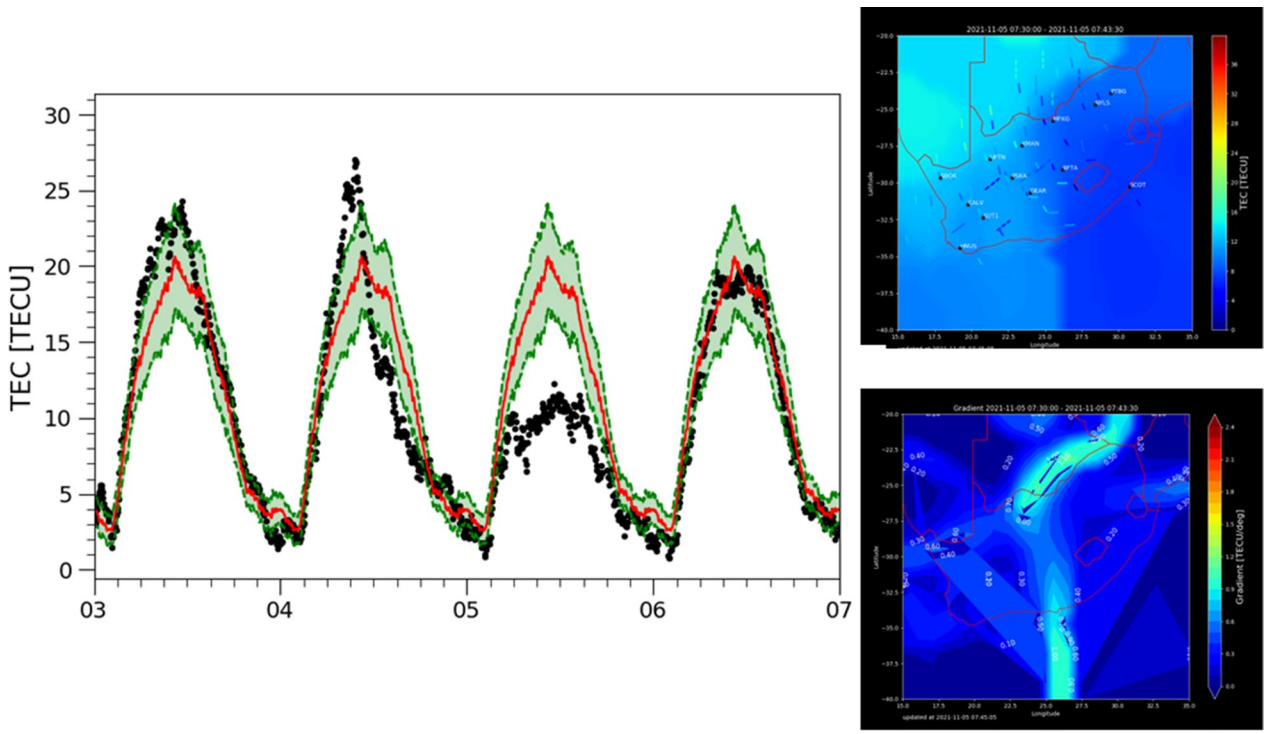

Background

Global Navigation Satellite System (GNSS) Total Electron Content (TEC) can be used to study the behaviour of the ionosphere during space weather events such as solar flares, Coronal Mass Ejections (CMEs), and Corotating Interaction Regions (CIRs). During a geomagnetic storm period, either a decrease or an increase in TEC (termed positive or negative ionospheric storm effects) can be observed depending on the driving mechanism of the storm (Matamba and Habarulema 2018). CIR-driven storms generally give positive ionospheric response (Burešová et al. 2014; Matamba and Habarulema 2018) and CME-driven storms may cause both enhancement and depression in TEC or negative ionospheric storm effect over mid-latitudes depending on season and onset time of the storm (Prölss 1995; Buonsanto 1999; Matamba et al. 2016; Matamba and Habarulema 2018; Wen and Mei 2020, and references therein). Burešová et al. (2014) studied the responses of the mid-latitude ionosphere to minor/moderate geomagnetic storms over the European sector and mostly observed positive ionospheric effects during CIR-driven storms. The paper concluded that the positive ionospheric effects are comparable to interplanetary CME-driven storms during high solar activities. Matamba and Habarulema (2018) did a statistical analysis of the CME- and CIR-driven storms over the African middle, low and equatorial latitudes and observed positive ionospheric storms during the main phase of the geomagnetic storm and negative storm effects in the recovering phase for the mid-latitude stations. Matamba et al. (2016) investigated the responses of the ionosphere during geomagnetic storms with Dst $\leq$ -350 nT, and noted a complex combination of both positive and negative ionospheric responses were observed over the European and African mid-latitude sectors depending on the season. Wen and Mei (2020) observed predominantly positive ionospheric storm effects over China during a strong geomagnetic storm with weak depletions in the recovery phase.

The negative ionospheric storm effects over the mid-latitude region have been attributed to processes such as changes in neutral composition (Prölss 1980, 1995) and Disturbance Dynamo Electric Field (DDEF) (Blanc and Richmond 1980; Sastri 1988). During a geomagnetic storm, energy is input into the ionosphere, which changes the parameters, such as composition, temperature and circulation (Rishbeth 1975; Rees et al. 1983; Pavlov and Buonsanto 1990; Richmond and Lu 2000;

Danilov 2001). The composition changes may expand from the high- to mid-latitude regions depending on the strength of the storm (Prölss 1980). In extreme storms, the changes may even reach the low-latitude regions (Prölss 1995).

The ionospheric F-region is primarily dominated by atomic oxygen (O^+) (Rishbeth and Garriott 1969). The decrease in O^+ and the increase in the molecular nitrogen (N_2) density combine to reduce the ionization density in the F-region hence, the depleted electron density or negative ionospheric response is observed (Prölss 1995). The negative ionospheric storm effect due to changes in the neutral gas composition is most clearly observed in the morning sector and may last for many hours and reach days during continued geomagnetic activity (Prölss et al. 1991). During strong geomagnetic storms over the southern and northern hemispheres mid-latitude over Africa and Europe, respectively, Matamba et al. (2016) found that the negative ionospheric storms were partly due to changes in neutral composition and the DDEF.

Additionally, Richmond and Lu (2000) noted that the ionospheric composition is altered by the travelling atmospheric disturbances emanating from the polar regions which can cause an ionospheric plasma density to be enhanced or depleted or redistributed by electric fields and winds. Fuller-Rowell et al. (1994) noted that the negative ionospheric storm effects can be due to the enhanced molecular nitrogen in regions of sunlight and hence, the strength of electron density depletion depends on the local time and the longitude of the sector during a geomagnetic storm.

On the other hand, the positive ionospheric storm over the mid-latitude region has been attributed to Travelling Ionospheric Disturbances (TIDs), the expansion of the equatorial ionization anomalies (termed as dayside ionospheric super-fountain effect) (Tsurutani et al. 2004; Katamzi and Habarulema 2014; Matamba et al. 2016), and Prompt Penetration Electric Fields (PPEF) (Huang et al. 2006; Tsurutani et al. 2008; Matamba et al. 2016). Positive ionospheric storms at mid-latitude have been linked to Travelling Atmospheric Disturbances (TADs) which manifest themselves in the ionosphere as TIDs. The TADs carry along the equatorward-directed meridional winds which cause an increase in the height of the F2 layer and may result in an increase in ionization density (Prölss 1995).

In this study, the ionospheric response during the largest storm of Nov 2021 will be evaluated in terms of the response that was observed using SANSA's near-real-time (NRT) TEC product (Matamba and Danskin 2022). Several estimates of TEC and ionospheric parameters are studied for the storm period.

Data and methods

Near-real-time (NRT) product

The GNSS data were provided by the National Geospatial Information (NGI), South Africa (TrigNet) using Networked Transport of Radio Technical Commission for Maritime Services (RTCM) via Internet Protocol (Ntrip). The 1-min Receiver INdependent EXchange (RINEX) files, satellite biases, historical receiver biases, and navigational files were used as input. The satellite biases were downloaded daily from the Center for Orbit Determination in Europe (CODE) website (http://www.aiub.unibe.ch/download/CODE/). The receiver biases are maintained at a fixed level for as long as possible. The receiver bias is only updated due to a change in the receiver.Matamba et al. (2020) indicated that the receiver bias varied typically up to ~0.8 TECU. Matamba and Danskin (2022) determined that the RMSE was typically from ~1.4 to ~2.8 TECU for the period May–Nov 2021.

The NRT TEC products were presented in Matamba and Danskin (2022) and are based on the method of Ma and Maruyama (2003) to estimate the daily receiver biases for the GNSS receivers. A map of the receiver's locations used in this paper is presented in Fig. 1. Normally, the TEC map product would be generated with 20 or more stations, however, during 3–8 Nov only 13 stations had near-real-time data. The NRT TEC maps are created every 5 min using the available data during the last 15 min.

TEC values with an elevation angle greater than 30° are considered for the TEC map in order to minimize the multi-path errors. The quality of the TEC map was calculated based on two methods, the first method is

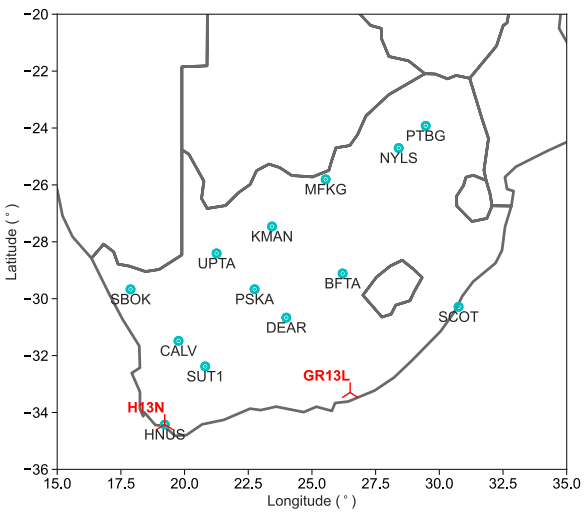

Fig. 1 Map indicating the available TrigNet GNSS stations (cyan dots) and ionosondes (red symbols) for the southern African region used in the study

the number of stations used divided by the total number of selected stations. The second method uses the number of valid TEC values divided by the total number of TEC values. Valid TEC values are greater than zero and have an elevation angle greater than 30°.

The error of the TEC maps was quantified using the root mean squared error (RMSE) determined between the map values and the measurements at the Ionospheric Pierce Points (IPPs). The spatial TEC gradient was estimated from the TEC map using the Scharr operator (Scharr 2000, 2007) as a gradient filter applied to the map image (Matamba and Danskin 2022). The TEC spatial gradient maps retained the 1°×1° latitude and longitude grid of the TEC maps.

Additionally, ionosonde TEC data from Hermanus (19.22°E, 34.42°S) and Grahamstown (26.50°E, −33.30°S) stations were compared with the quiet-time AfriTEC model (Okoh et al. 2019, 2020) and the TEC values extracted from the maps. The ionosonde TEC is calculated from the electron density profile up to 1000 km as derived from ionosonde measurements. The electron density profile is a combination of the inverted bottom-side ionogram (up to the height of the F2 peak) and a modelled topside profile (Huang and Reinisch 2001; McKinnell et al. 2007). The auto-scaled values of TEC from the ionograms were used for the analysis since the measurements are done in near-real-time. The quiet-time AfriTEC model is a model based on a neural network ionospheric model over Africa (Okoh et al. 2019) dependent on solar radio flux at 10.7-cm wavelength (F10.7).

Thermospheric O/N_2 ratio data

The thermospheric O/N_2 ratio maps were downloaded from Thermosphere Ionosphere Mesosphere Energetics and Dynamics/Global Ultraviolet Imager (TIMED/GUVI) website (http://guvitimed.jhuapl.edu/guvi-gallery3on2). TIMED is used to study the energetics and dynamics of the mesosphere and lower thermosphere between an altitude of approximately 60 to 180 kms (http://guvitimed.jhuapl.edu/). The approximate time for the GUVI overpasses are 07:56, 07:46, and 07:36 UT over the African region on 3–5 Nov 2021.

Geomagnetic conditions

In Fig. 2, the Dst and Kp index values for 3–8 Nov were obtained from World Data Center for Geomagnetism, Kyoto (http://wdc.kugi.kyoto-u.ac.jp/wdc/Sec3.html) and the Helmholtz Centre Potsdam—GFZ German Research Centre for Geosciences (https://kp.gfz-potsdam.de/en/), respectively. Figure 2 illustrates the Kp as a bar graph with green, yellow, and red bars indicating quiet, active, and stormy periods, respectively, and the Dst index as a black line. The minimum Dst occurred (-125 nT) on 4 Nov at 13:00 UT and Kp reached a maximum of 7+ between 09:00 and 12:00 UT. The recovery phase of the geomagnetic storm started after 4 Nov at 13:00 UT.

On 5 Nov the Kp index was mainly unsettled throughout the day and on 6 and 7 Nov two intervals of Kp =

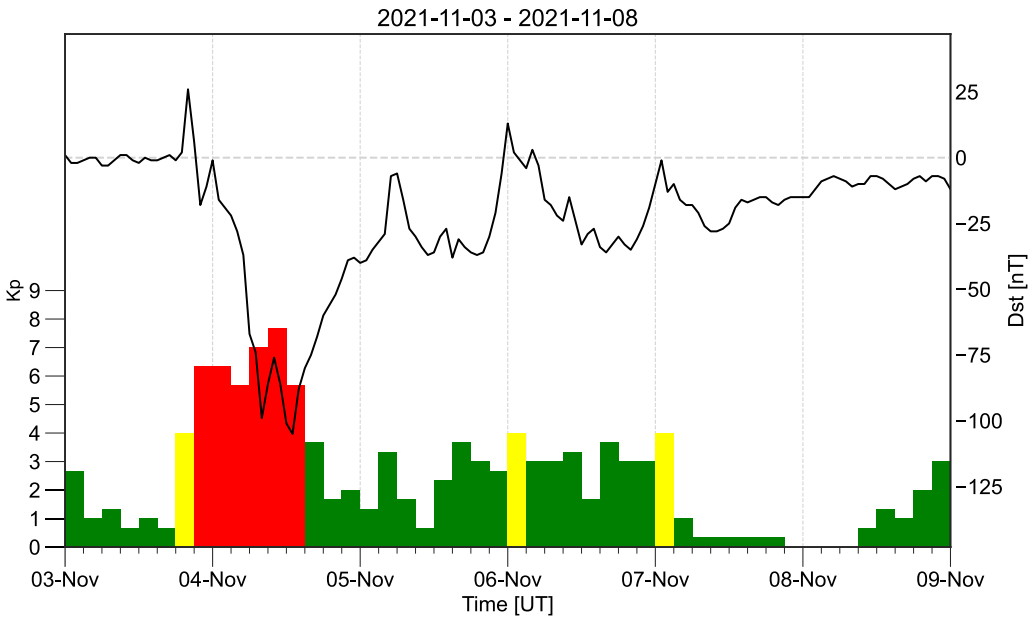

Fig. 2 Dst and Kp indices for the 3–8 Nov 2021. The colour of the bar for the Kp-index is green, yellow, and red for Kp < 4, between 4 and 5, and > 5, respectively. The green, yellow, and red bars represent quiet, active, and storm periods, respectively, as defined by Kp

4 were observed between 0:00–3:00 UT. After the Kp=4, the Dst index showed a decrease for several hours afterwards Kp indicated quiet levels after 7 Nov 3:00 UT.

Results

Figure 3 shows the NRT TEC maps at 07:30 UT (09:30 LT) for 3–8 Nov. Figure 3a is the day before the storm while (b) and (c) are during the storm and (d), (e) and (f) are in the recovery phase. The receiver locations are indicated with black dots and the station codes are in white. The TEC values at IPP are plotted on the maps with the same colour scale as the background TEC. The background TEC is the contoured fit to the median-filtered verticalized TEC. Often the TEC at IPP blends well with the background TEC visually indicating that the modelled TEC fits the measurements well. Sometimes, differences between the model and the measurements are noticeable, such as in Fig. 3c. The noticeable difference is an indication that the TEC is not uniformly distributed or the presence of spatial gradients.

The update time, RMSE, and quality of the TEC maps are indicated below each figure. The maximum RMSE value for the maps of Fig. 3 is 2.63 TECU on 4 Nov. An increase in TEC on 4 Nov to ~32 TECU in the northern part of the map as compared with the 3 Nov was observed during the first decrease of Dst. A decrease in TEC was observed on 5 Nov over the entire map in comparison with TEC values observed on 3 (before the storm), 6–8 (recovery phase) Nov.

The change in TEC during the geomagnetic storm period was also tracked using the TEC data from ionosondes at Hermanus and Grahamstown as shown in Fig. 4 with red dots. Figure 4a and b contains the temporal variation of TEC extracted from the NRT TEC maps (black dots) over the ionosonde locations. In addition, the quiet-time AfriTEC model is displayed for both ionosonde locations as a green line in the respective panel. The TEC from ionosonde was computed by Artist 5 software in near-real-time autoscaling procedure of the digisonde. The ionosonde data were not manually edited as the product is required in near-real time. The quiet-time AfriTEC model is used as a guide to the expected level of TEC in the absence of any storm effects.

The dashed vertical lines in Fig. 4a and b correspond to the approximate time of the GUVI overpasses at 7:56, 7:46, 7:36, 7:26, 7:16, and 7:07 UT on 3–8 Nov, respectively. An afternoon depression was observed from 3–7 Nov for both Hermanus and Grahamstown stations as compared with the quiet time AfriTEC model. On 5 Nov a significant decrease in TEC of ~50% was observed over Grahamstown and Hermanus. The depression in TEC is clearly observed on 4 and 5 Nov in both the near-real-time and ionosonde TEC.

Fig. 5 illustrates the spatial TEC gradient for 3–8 Nov at the same period as the TEC maps. The TEC gradient values range of less than 0.5 TECU/deg can be considered insignificant. The gradient values are written next to the contours within the map. The highest gradients are observed in Fig. 5b and c during the storm period. On 4 Nov (Fig. 5b), the largest gradient (~1.5 TECU) was observed across the northern part of South Africa extending from the east to the west of the map. As observed in Fig. 3b, the TEC values were lowest over the southern part of South Africa and highest over the northern part of the map. The TEC values at IPPs do not agree well with the background TEC over the North whereas, in the southern region, the TEC values blend with the background.

In Fig. 5c, a north-to-south (N–S) gradient is observed and happens to lie between Hermanus and Grahamstown. The TEC map (Fig. 3c) corresponding to the enhanced gradient shows depleted TEC values on the east part during the sunrise and enhanced TEC values were observed on the west. The TEC at IPPs does not blend well with the background on the western part of the map, whereas a good agreement is observed on the east part of the map. Hence, the gradients show substantial (>1.0 TECU/deg) ionospheric variability during the geomagnetic storm.

Figure 5a, d, e, and f's TEC gradient is below 0.5 TECU/deg when measurements are within 300 km of GNSS receivers marked in black dots in Fig. 3. Artefacts can occur in the mapping process as no receivers are available (typically outside the South African boundaries for the presented TEC maps). Figure 5a is before the geomagnetic storm and Fig. 5d, e, and f is during the recovery phase of a geomagnetic storm. Before and after the storm, the TEC values at IPP blend very well with the background and often the TEC measurements cannot be distinguished from the background.

Discussion

The depression in TEC has often been related to a decrease in the O/N_2 ratio as discussed by numerous authors (e.g., Prölss 1980, 1993, 1995; Zhang et al. 2003; Matamba et al. 2016). The thermospheric O/N_2 ratio was obtained from Global UltraViolet Imager (GUVI) (Zhang et al. 2004). GUVI is a far ultraviolet scanning spectrograph imager that provides horizon-to-horizon images in five selectable wavelength intervals (HI 121.6 nm, OI

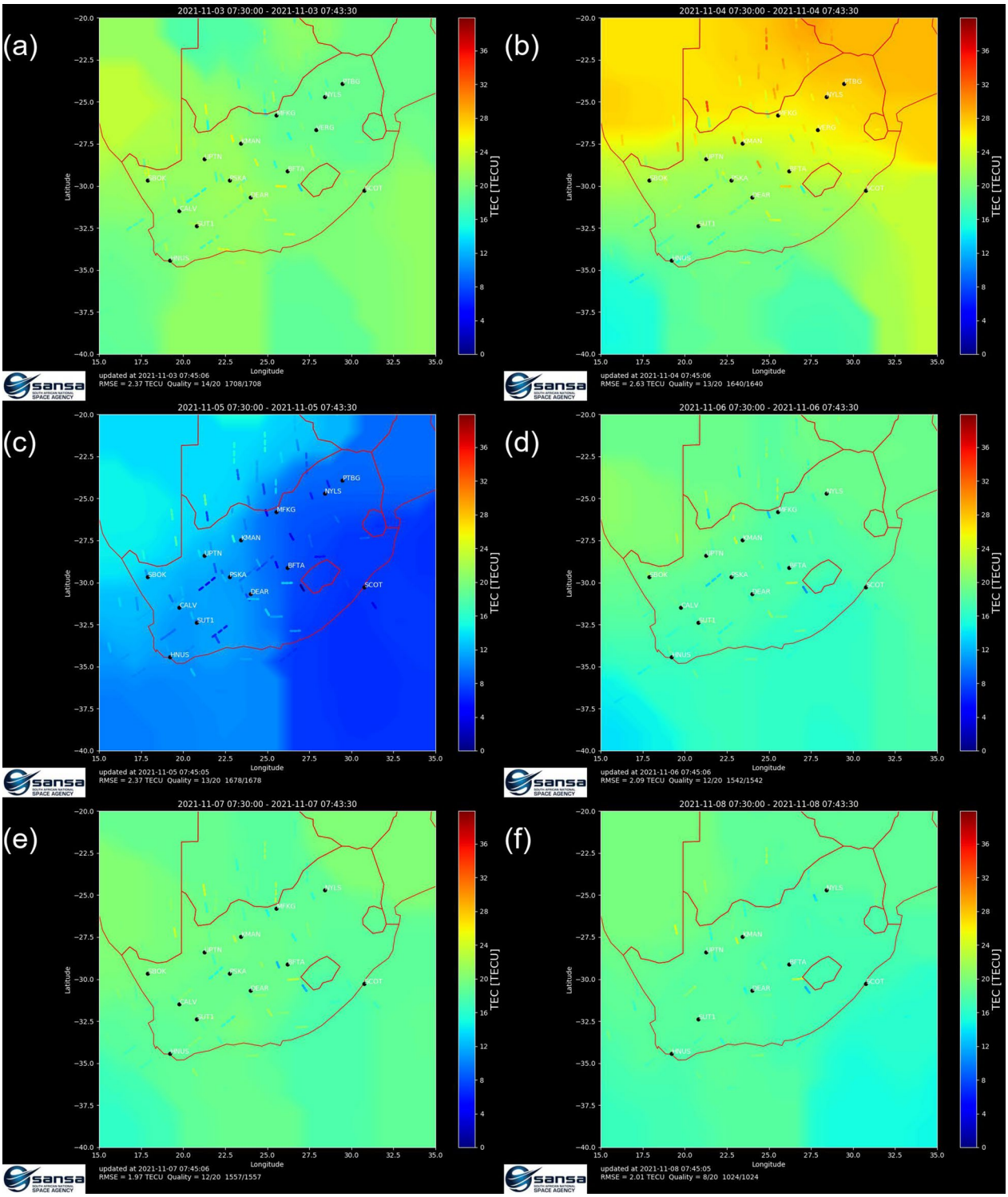

Fig. 3 Total electron content (TEC) maps for the period 3–8 Nov 2021 at 07:30–07:43 UT are shown in panels **a**–**f**, respectively. The black dots represent the station location and the station name is labelled in white. The TEC at IPP is plotted as a scatter using the same colour bar as the background TEC map

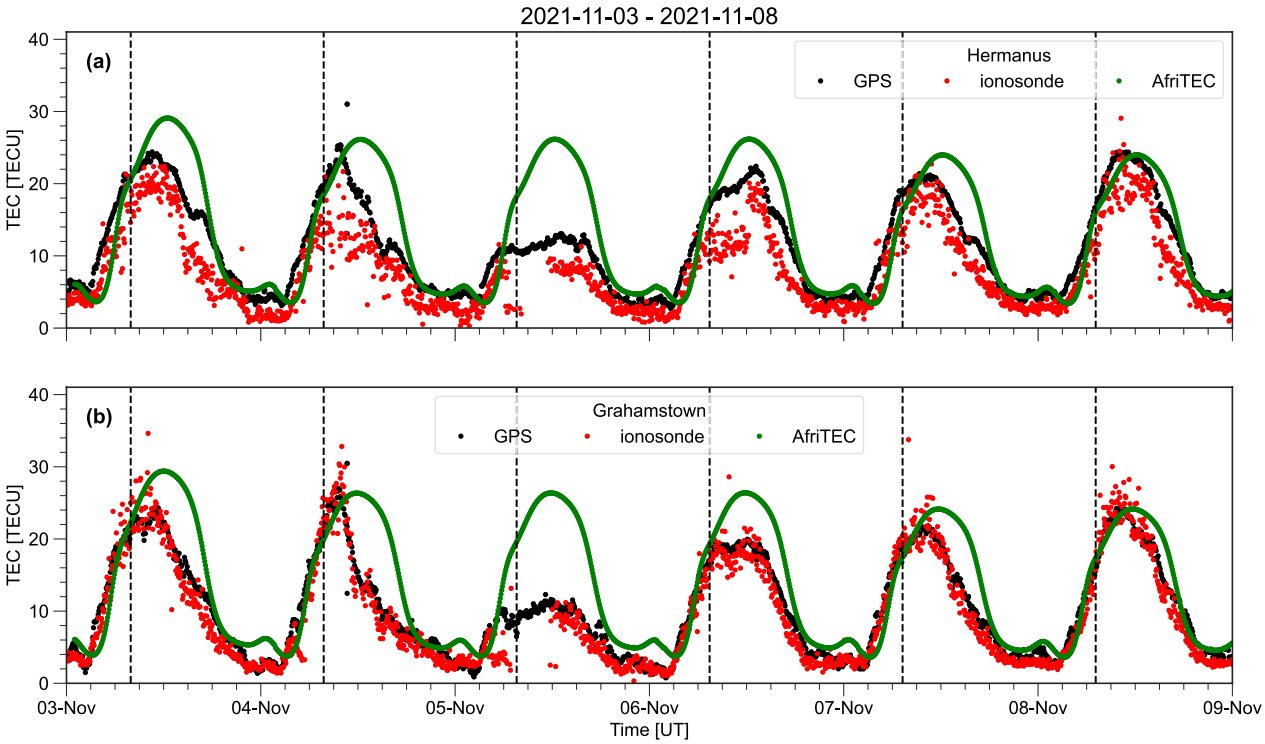

Fig. 4 **a** and **b** are the variation of TEC from GPS, ionosonde, and AfriTEC models for Hermanus and Grahamstown, respectively, for the period 3–8 Nov 2021. The vertical dashed lines correspond to the time of the GUVI overpasses at 7:56, 7:46, 7:36, 7:26, 7:16, and 7:07 UT on 3–8 Nov 2021, respectively

130.4 nm, OI 135.6 nm, and N_2 Lyman–Birge–Hopfield bands 140 to 150 nm and 165 to 180 nm).

The TEC maps in Fig. 3 were selected for comparison with the GUVI measurement of the O/N2 ratio between ~7:30 - ~7:59 UT. Figure 6 illustrates O/N_2 ratio before (3 Nov) and during (4–5 Nov) the geomagnetic storm. Since the GUVI product is estimated for ~9:30 LT, over South Africa the time is approximately 7:30 UT. The O/N_2 ratio was ~0.6 over the South African region on 3 Nov. The decrease in TEC was observed after 10:00 UT on 4 Nov on both the TEC maps and ionosondes. Figure 6(b) has O/N_2 ratio less than 3 Nov, but not as depressed as on 5 Nov. Figure 6(c) indicates that O/N_2 ratio is substantially reduced as compared with 3 Nov. A decrease in O/N_2 ratio to ~0.4 was observed covering the South African region on 5 Nov. The decrease in the O/N_2 ratio on 5 Nov from GUVI coincided with the depression in observed TEC over South Africa occurring at the same time as the N–S gradient of TEC between Hermanus and Grahamstown. The TEC decreased by ~50% from the typical TEC values. Negative ionospheric storm effects are due to the changes in neutral gas composition which are advected toward mid-latitudes during the night and afterwards rotate into the day sector (Prölss 1993).

Previous researchers have observed that the ionospheric electron density in the mid-latitude may be reduced by a factor of 2–5 (50–80%) during negative storm effects (Prölss 1980; McNamara 1991; Strickland et al. 2001; Zhang et al. 2003). During a geomagnetic storm, the magnetospheric energy input to the atmosphere at the auroral latitudes is greatly enhanced. Wang et al. (2021) showed that during geomagnetic storms, Joule heating can cause the thermospheric density to enhance in the higher-latitude areas. Increased Joule heating at high latitudes reduces the normal poleward wind on the dayside and reinforces the regular equatorward wind on the night side and creates a storm circulation that can transport air with increased molecular species to mid-latitudes. The neutral composition disturbances move to lower latitudes, and the enhanced loss rate will result in significant decreases in the F region electron density (Zhang et al. 2003, 2004).

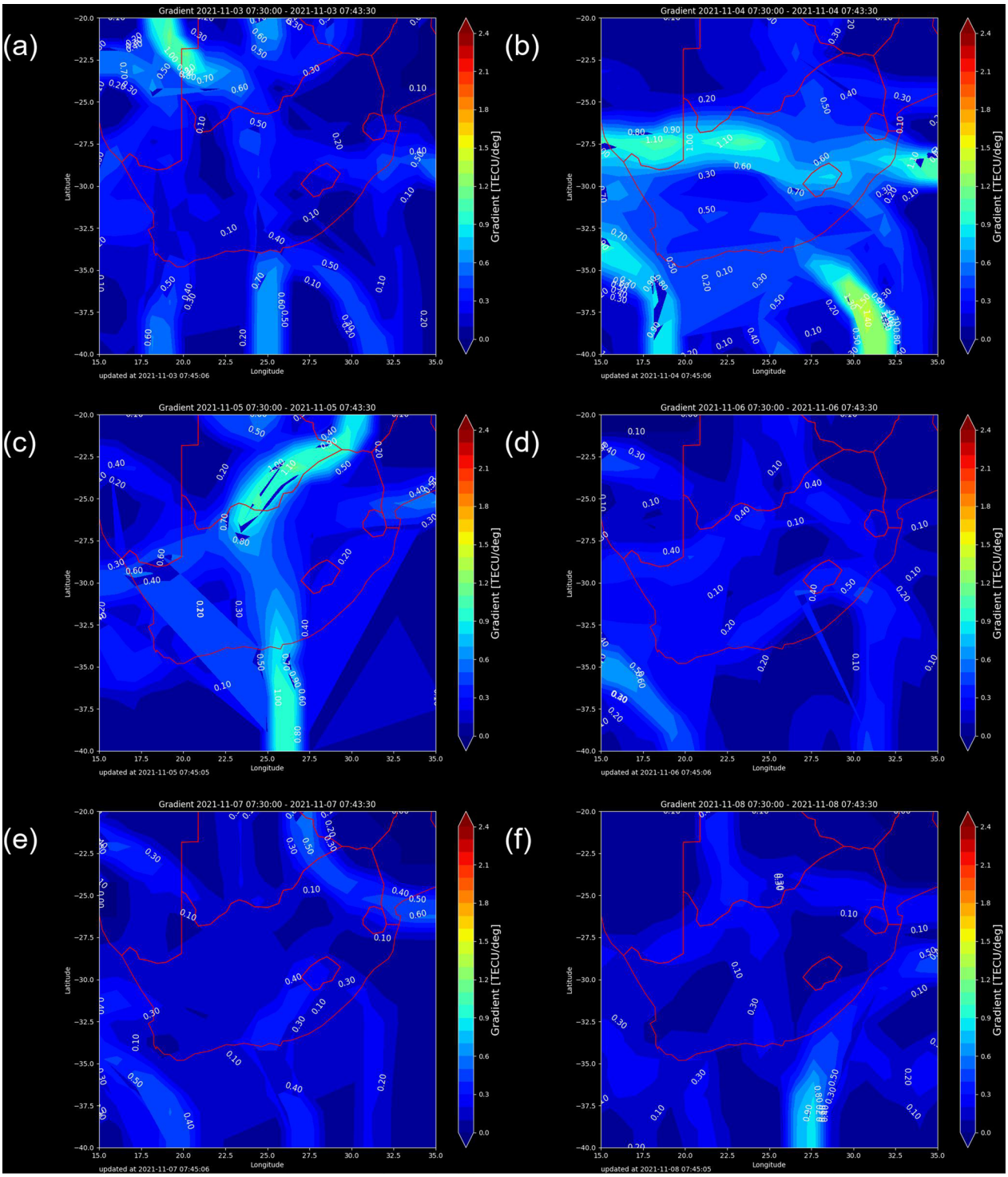

Fig. 5 Total electron content (TEC) spatial gradient maps for 3–8 Nov 2021 storm period are shown in panels **a**–**f**, respectively.

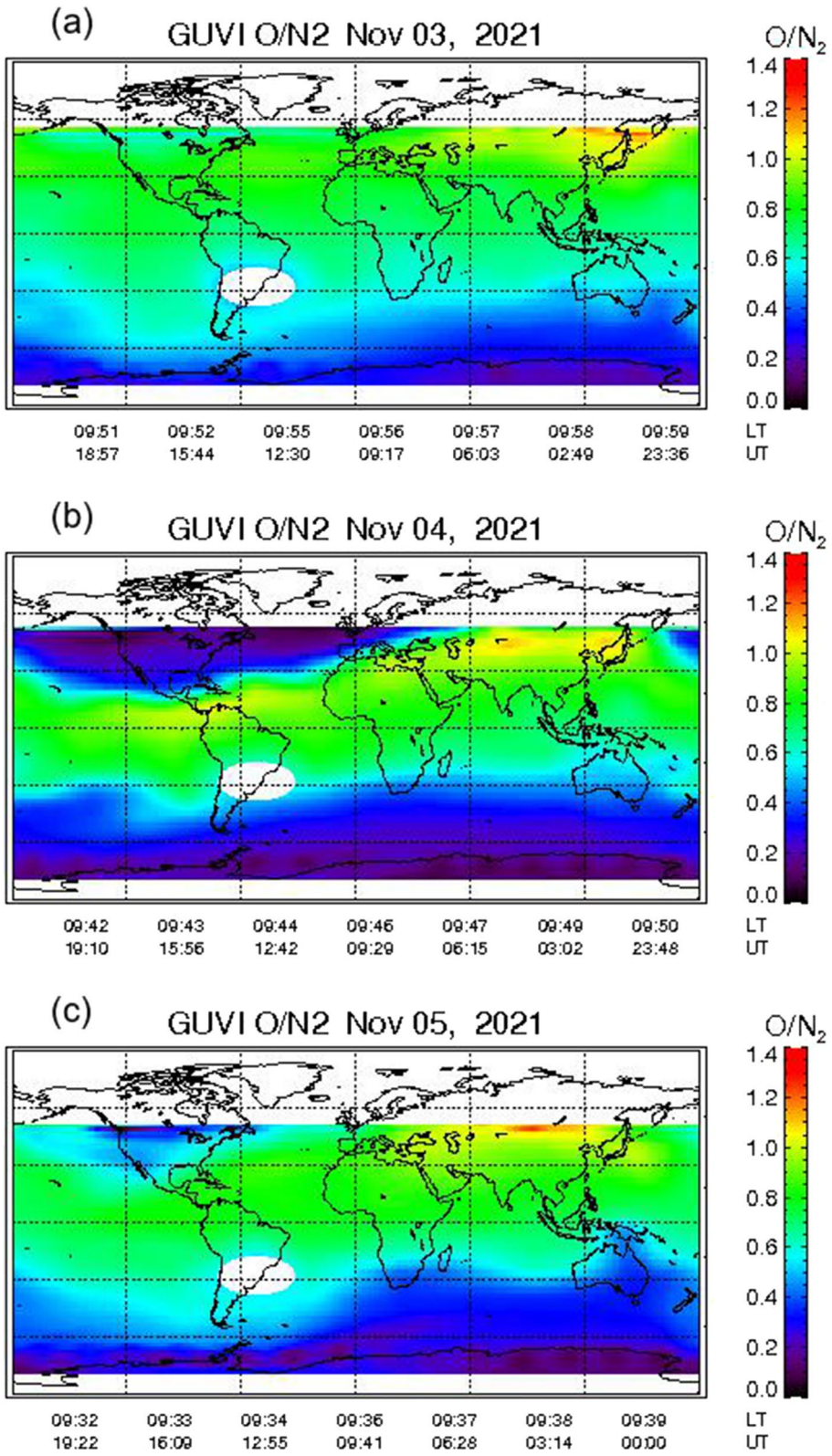

Fig. 6 GUVI O/N_2 ratio plots for 3, 4 and 5 Nov 2021 are shown in panels **a**, **b** and **c**, respectively

Conclusions

In this paper, the TEC over South Africa has been studied during a geomagnetic storm on 3–8 Nov 2021. A decrease in TEC was observed on 4 and 5 Nov in both Hermanus and Grahamstown ionosondes as well as in the NRT TEC maps as compared with the AfriTEC quiet time model. The decrease in TEC may be related to the depletion of the O/N_2 ratio on the 4–5 Nov 2021 daytime hours. The GUVI O/N_2 ratio shows a substantial decrease on 5 Nov during the recovery phase of the storm as compared with the day before the storm.

Substantial gradients (gradients greater than 1.0 TECU/deg) were observed over the region during the storm period. The ionosondes at Hermanus and Grahamstown were on opposite sides of the gradient on 5 Nov. The ionosphere was depleted more over Grahamstown rather than Hermanus at 7:30 UT (∼9:30 LT), which is during the morning period. Normally, in the morning time sector, Grahamstown should have higher TEC than Hermanus based on the solar zenith angle.

Acknowledgements

The GUVI data used here are provided through support from the NASA MO &DA program. The GUVI instrument was designed and built by The Aerospace Corporation and Johns Hopkins University. The Dst used in this paper was provided by the WDC for Geomagnetism, Kyoto (http://wdc.kugi.kyoto-u.ac.jp/wdc/Sec3.html). The satellite bias data were obtained from http://www.aiub.unibe.ch/download/CODE/. The South African GNSS data were provided by the Chief Directorate: National Geo-spatial Information, South Africa (http://trignet.co.za/) via NTRIP. The ionosonde data can be obtained from https://giro.uml.edu/didbase/. The authors would also like to thank SANSA for the NRT ionosonde and GNSS data.

Author contributions

TMM and DWD wrote the manuscript based on the TEC map product. MT and RN reviewed and improved the manuscript with numerous suggestions for improvements.

Funding

This work is based on the research supported in part by the National Research Foundation (NRF) of South Africa for grant 148779; any opinion, finding, and conclusion or recommendation expressed in this material are that of the author(s), and the NRF does not accept any liability in this regard.

Availability of data and materials

GUVI data are available at http://guvitimed.jhuapl.edu/. Dst data are available at http://wdc.kugi.kyoto-u.ac.jp/wdc/Sec3.html. The satellite bias data were obtained from http://www.aiub.unibe.ch/download/CODE/. The South African GNSS data can be found at http://trignet.co.za/. The ionosonde data can be obtained from https://giro.uml.edu/didbase/.

Declarations

Competing interests

None.

Author details

[1]South African National Space Agency (SANSA), Hermanus 7200, South Africa.

Received: 22 May 2023 Accepted: 1 September 2023
Published online: 19 September 2023

References

Blanc M, Richmond AD (1980) The ionospheric disturbance dynamo. J Geophy Res 85(A4):1669

Buonsanto MJ (1999) Ionospheric storms - a review. Space Sci Rev 88(3–4):563–601

Burešová D, Laštovička J, Hejda P, Bochnicek J (2014) Ionospheric disturbances under low solar activity conditions. Adv Space Res 54:185–196

Danilov AD (2001) F2-region response to geomagnetic disturbances. J Atmosph Solar-Terrestrial Phys 63:441–449

Fuller-Rowell TJ, Codrescu MV, Moffett RJ, Quegan S (1994) Response of the thermosphere and ionosphere to geomagnetic storms. J Geophy Res Space Phys 99:3893–3914

Habarulema JB, Katamzi-Joseph ZT, Burešová D, Nndanganeni R, Matamba T, Tshisaphungo M, Buchert S, Kosch M, Lotz S, Cilliers P et al (2020) Ionospheric response at conjugate locations during the 7–8 September 2017 geomagnetic storm over the Europe-African longitude sector. J Geophy Res Space Phy 125(10):e2020JA028307

Huang X, Reinisch BW (2001) Vertical electron content from ionograms in real-time. Radio Sci 36(2):335–342

Huang C, Sazykin I, Spiro R, Goldstein J, Crowley G, Ruohoniemi JM (2006) Storm-time penetration electric fields and their effects. Eos Trans AGU 87(13):131–131. https://doi.org/10.1029/2006EO130005

Katamzi ZT, Habarulema JB (2014) Traveling ionospheric disturbances observed at South African midlatitudes during the 29–31 October 2003 geomagnetically disturbed period. Adv Space Res 53(1):48–62

Ma G, Maruyama T (2003) Derivation of TEC and estimation of instrumental biases from GEONET in Japan. Anna Geophys 10:2083–2093

Matamba TM, Danskin DW, Cilliers PJ (2020) Evaluation of stability of GPS satellite and receiver bias. In 2020 IEEE International Conference on Wireless for Space and Extreme Environments (WiSEE) (pp. 78–82). https://doi.org/10.1109/WiSEE44079.2020.9262687

Matamba TM, Danskin DW (2022) Development and evaluation of near real-time TEC and ancillary products for SANSA space weather. Space Weather 20:e2021SW003013

Matamba TM, Habarulema JB, Burešová D (2016) Midlatitude ionospheric changes to four great geomagnetic storms of solar cycle 23 in Southern and Northern Hemispheres. Space Weather 14:1155–1171. https://doi.org/10.1002/2016SW001516

Matamba TM, Habarulema JB (2018) Ionospheric responses to CME- and CIR-driven geomagnetic storms along 30°E–40°E over the African sector from 2001 to 2015. Space Weather 16:538–556. https://doi.org/10.1029/2017SW001754

McKinnell LA, Opperman B, Cilliers PJ (2007) GPS TEC and ionosonde TEC over Grahamstown, South Africa: first comparisons. Adv Space Res 39(5):816–820

McNamara LF (1991) The ionosphere: communications, surveillance, and direction finding. Krieger Publishing Company, Malabar, Florida

Nava B, Rodríguez-Zuluaga J, Alazo-Cuartas K, Kashcheyev A, Migoya-Orué Y, Radicella SM, Amory-Mazaudier C, Fleury Rolland (2016) Middle-and low-latitude ionosphere response to 2015 St. Patrick's Day geomagnetic storm. J Geophy Res Space Phys 121(4):3421–3438

Okoh D, Seemala G, Rabiu B, Habarulema JB, Jin S, Shiokawa K et al (2019) A neural network-based ionospheric model over Africa from constellation observing system for meteorology, ionosphere, and climate and ground global positioning system observations. J Geophys Res Space Phy 124(12):10512–10532

Okoh D, Habarulema JB, Rabiu B, Seemala G, Wisdom JB, Olwendo J et al (2020) Storm-Time modeling of the African regional Ionospheric total electron content using artificial neural networks. Space Weather 18(9):e2020SW002525

Pavlov AV, Buonsanto MJ (1990) Comparison of model electron densities and temperatures with Millstone Hill observations during undisturbed periods and the geomagnetic storms of 16–23 March and 6–12 April 1990. Anna Geophys 15:327–344

Prölss GW (1980) Magnetic storm associated perturbations of the upper atmosphere: recent results obtained by satellite-borne gas analyzers. Rev Geophy 18(1):183–202

Prölss GW, Brace LH, Mayr HG, Carignan GR, Killeen TL, Klobuchar JA (1991) Ionospheric storm effects at subauroral latitudes: a case study. J Geophy Res space physics 96(A2):1275–1288

Prölss GW (1993) On explaining the local time variation of ionospheric storm effects. Anna Geophy 11(1):1–9
Prölss GW (1995) Ionospheric F-region storms, in Handbook of atmospheric electrodynamics. In: Volland H (ed) CRC Press. Fla, Boca Raton, pp 195–248
Rees MH, Emery BA, Roble RG, Stamnes K (1983) Neutral and ion gas heating by auroral electron precipitation. J Geophy Res Space Phy 88(A8):6289–6300
Richmond AD, Lu G (2000) Upper-atmospheric effects of magnetic storms: a brief tutorial. J Atmosp Solar-Terrestrial Phy 62(12):1115–1127
Rishbeth H, Garriott OK (1969) Introduction to ionospheric physics. ACADEMIC PRESS INC., New York and London
Rishbeth H (1975) F-region storms and thermospheric circulation. J Atmosp Solar-Terrestrial Phy 37(6–7):1055–1064
Sastri JH (1988) Equatorial electric fields of ionospheric disturbance dynamo origin. Anna Geophys 6(6):635–642
Scharr H (2000) Optimal operators in digital image processing. Dissertation, University of Heidelberg, https://doi.org/10.11588/heidok.00000962
Scharr H (2007) Optimal Filters for Extended Optical Flow. In: "Jähne B, Mester R, Barth E, Scharr H (eds) Complex Motion. IWCM 2004. Lecture Notes in Computer Science, vol 3417. Springer, Berlin, Heidelberg. https://doi.org/10.1007/978-3-540-69866-1_2
Strickland DJ, Daniell RE, Craven JD (2001) Negative ionospheric storm coincident with DE 1-observed thermospheric disturbance on October 14, 1981. J Geophy Res 106(A10):21049–21062. https://doi.org/10.1029/2000JA000209
Tsurutani B, Mannucci A, Iijima B, Abdu MA, Sobral JHA, Gonzalez W, Guarnieri F, Tsuda T, Saito A, Yumoto K, Fejer B (2004) Global dayside ionospheric uplift and enhancement associated with interplanetary electric fields. J Geophy Res. https://doi.org/10.1029/2003JA010342
Tsurutani BT, Verkhoglyadova OP, Mannucci AJ, Saito A, Araki T, Yumoto K, Tsuda T, Abdu MA, Sobral JHA, Gonzalez WD, McCreadie H (2008) Prompt penetration electric fields (PPEFs) and their ionospheric effects during the great magnetic storm of 30–31 October 2003. J Geophy Res Space Phy. https://doi.org/10.1029/2007JA012879
Wang X, Miao J, Lu X, Aa E, Liu J, Wang Y, Liu S (2021) Latitudinal impacts of Joule heating on the high-latitude thermospheric density enhancement during geomagnetic storms. J Geophy Res Space Phy 126:e2020JA028747. https://doi.org/10.1029/2020JA028747
Wen D, Mei D (2020) Ionospheric TEC disturbances over China during the strong geomagnetic storm in September 2017. Adv Space Res 65(11):2529–2539
Zhang YL, Paxton J, Kil H, Meng C-I, Mende SB, Frey HU, Immel TJ (2003) Negative ionospheric storms seen by the IMAGE FUV instrument. J Geophy Res 108(A9):1343. https://doi.org/10.1029/2002JA009797
Zhang Y, Paxton LJ, Morrison D, Wolven B, Kil H, Meng C-I, Mende SB, Immel TJ (2004) O/N_2 CDATA changes during 1–4 October 2002 storms: IMAGE SI-13 and TIMED/GUVI observations. J Geophy Res 109:A10308. https://doi.org/10.1029/2004JA010441

Publisher's Note